Available online at www.sciencedirect.com
ScienceDirect
Journal of Nuclear Materials 372 (2008) 16–31
journal of nuclear materials
www.elsevier.com/locate/jnucmat

Radiation damage effects in candidate titanates for Pu disposition: Zirconolite

D.M. Strachan *, R.D. Scheele, E.C. Buck, A.E. Kozelisky, R.L. Sell, R.J. Elovich, W.C. Buchmiller

Pacific Northwest National Laboratory, 902 Battelle Boulevard, P.O. Box 999, Richland, WA 99352, USA

Received 15 August 2006; accepted 23 January 2007

Abstract

Results from studies of radiation-induced damage from the alpha decay of ^{238}Pu on the density and crystal structure of a nominally phase-pure zirconolite and two other zirconolite-bearing ceramics are discussed. Macro and micro swelling were found to be temperature independent, whereas the density determined with He gas pycnometry was temperature dependent. Approximately 2.6×10^{18} α/g were needed to render the specimens X-ray amorphous– more to saturate the swelling. Unlike pyrochlore-based ceramics, we did not observe any phase changes associated with storage temperature and damage ingrowth. The forward dissolution rate at a pH value of 2 for material containing essentially all zirconolite is $1.7(4) \times 10^{-3}$ g/(m^2 d) with very little pH dependence and no dependence on the amount of radiation-induced damage. Even after the radiation-induced swelling saturated, the specimens remained physically intact with no evidence for microcracking. Thus, the material remains physically a viable material for the disposition of surplus weapons-grade Pu.

1. Introduction

This is the second of two articles in which the results from the studies of the radiation-induced damage effects from the self irradiation with ^{238}Pu are reported. Introductory material has been presented in a previous paper [1] and is not repeated here. In a previous article [1], we discussed the effects of radiation-induced damage on one of the main crystalline phases, pyrochlore (betafite), in the ceramics that were developed for the disposal of weapons-grade plutonium. In this article, we discuss the effects of radiation-induced damage on the other main crystalline phase, zirconolite (ideally $CaZrTi_2O_7$), that was also being developed as a phase in which to sequester Pu from surplus nuclear weapons. As part of the development of crystalline waste forms for high-level nuclear waste from reactor fuel reprocessing, zirconolite began to receive attention in the late 1970s as a phase in which actinides could be immobilized [2–4]. In the latter case, the Synroc waste form received and continues to receive attention as a potential waste form, in particular for actinides. Most of the recent work on Synroc is by the scientists from the group at the Australian Science and Technology Organisation (ANSTO) near Sydney. The basis of the Synroc waste form is that it is composed of phases that have existed in nature for millennia.

Lumpkin [5] has written an extensive review article on the alpha-decay damage in four mineral phases: zirconolite, pyrochlore, perovskite, and brannerite. Three of these (pyrochlore, zirconolite, and brannerite) may be found in an immobilized plutonium form. The ideal chemical formula for zirconolite is $CaZrTi_2O_7$. However, many elements can be substituted on the Ca [rare-earth elements (REEs), Th, U, Mn, and Sr], Zr [Ti, REE, Hf, Pu, and U], and Ti [Mg, Fe(II), Fe(III), Nb, Pu, Al, Cr, Mn, Zn, Ta, W] sites. Many of these substitutions are also found in natural zirconolites [6]. Zirconolites are chemically durable, having survived in nature for several hundred million years. Ringwood et al. [7] showed that U in zirconolites

* Corresponding author.
E-mail address: denis.strachan@pnl.gov (D.M. Strachan).

0022-3115/$ - see front matter © 2007 Elsevier B.V. All rights reserved.
doi:10.1016/j.jnucmat.2007.01.278

that were ca. 500 million years old from Sri Lanka was still present, even though the samples were from stream-bed gravels that remained after the host rock had been completely altered, indicating extensive contact with water. These specimens were completely X-ray amorphous from alpha-decay damage. Significant alteration in natural zirconolites is usually found in geologic sites where temperatures in excess of 500 °C and hydrothermal conditions existed [7].

Natural zirconolites accumulate doses of 1×10^{19} α/g to become fully amorphous [6,7]. In synthetic zirconolites, the dose at which swelling and other macroscopic properties cease to exhibit detectable change is lower than in natural zirconolites and ranges from 4.3×10^{18} α/g for $CaPuTi_2O_7$ (cubic zirconolite structure) [8–10] to $>9 \times 10^{17}$ α/g for monoclinic zirconolite [8]. The dose at which the synthetic specimens become X-ray amorphous is substantially less than the dose at which swelling saturates. For example, Clinard et al. [9] report for cubic zirconolite an X-ray amorphous dose of 8×10^{17} α/g. Weber and Matzke [10] and Weber et al. [11] report that zirconolite with about 3 mass% ^{244}Cm became X-ray amorphous at 2.1×10^{25} α/m^3 (4.2×10^{18} α/g) and amorphous to selected-area electron diffraction in a transmission electron microscope at 2.3×10^{25} α/m^3 (4.6×10^{18} α/g) while the specimen still exhibited swelling at 2.4×10^{25} α/m^3 (4.8×10^{18} α/g).

The effect of temperature on critical dose (dose needed for the sample to become amorphous) in natural zirconolite has been investigated by Lumpkin [12]. He calculated that an increase in storage temperature from 50 °C to as much as 200 °C increases the dose required to render a zirconolite amorphous by a factor of three. He also found that the change with temperature depends on the composition of the zirconolite. The temperature effect on critical dose in synthetic zirconolites has been measured by Clinard et al. [13] with ^{238}Pu-bearing cubic zirconolite and by many authors with heavy ion bombardment (for example, [14–16]). However, the critical temperature – the temperature at which the damage is annealed at the same rate as it occurs – depends on the mass of the bombarding ion [14]. For $CaZrTi_2O_7$, the critical temperature is in the range of 325–425 °C. The dependence on temperature is insignificant up to 25 °C below the critical temperature.

In this publication, we report on the effects of radiation damage on the density and crystal structure of nominally 'phase pure' zirconolite specimens and specimens in which the main crystalline phase is zirconolite. The latter were developed to accomodate the chemical variability in the Pu feed to a proposed immobilization plant. We also report on the chemical durabilty of the zirconolite phase and compare it with the pyrochlore phase reported in our previous paper [1].

2. Experimental methods

Leading up to the preparation of the test specimens, we prepared numerous samples from non-radioactive components, namely Ce, Hf, and Gd. The latter two were also included in the actual formulations because they act as neutron absorbers to prevent nuclear criticality in the actual materials to be disposed and their alteration products. Three zirconolite-bearing materials were prepared to represent those ceramic materials that would have been made at the proposed Plutonium Immobilization Plant [17,18]. The ceramic specimens were not analyzed for composition; the target compositions for Z1, ZB1, and ZIB1 are shown in Table 1. Molybdenum was added to the formulation to serve as an indication of the behavior of the matrix in the dissolution experiments. Each specimen represented a potential product of the plant: Z1, a nominally pure zirconolite; ZB1, a material most likely to be produced at the plant; and ZIB1, a product that would result if all the impurities in the Pu feed were to be included in a single ceramic product.

Between characterization and testing that occurred approximately semiannually, the specimens were housed in argon-filled stainless-steel vessels in ovens. Each vessel contained either three (^{239}Pu-bearing) or four specimens

Table 1
The target oxide composition of the ^{238}Pu- and ^{239}Pu-bearing zirconolite ceramics used in this study

Component	Z1		ZB1		ZIB1		Impurities		
	mass%	mole%	mole%	mass%	mole%	mass%	Component	mole%	mass%
$Al(OH)_3$	1.74	1.97	1.3	1.12	0.58	0.50	B_2O_3	0.29	0.17
CaO	10.2	21.03	19.8	9.06	19.95	9.44	$CaCl_2$	0.71	0.66
Gd_2O_3	2.06	0.66	2.2	6.56	2.47	7.54	CaF_2	0.67	0.44
HfO_2	43.08	23.66	13.8	23.80	5.67	10.07	Cr_2O_3	0.07	0.09
MoO_3	0.1	0.09	0.1	0.11	0.26	0.28	Fe_2O_3	0.11	0.15
PuO_2	7.4	3.17	4.9	10.92	4.94	11.26	Ga_2O_3	0.36	0.57
TiO_2	33.61	48.63	50.9	33.28	50.51	34.03	K_2O	0.40	0.32
UO_2	1.81	0.79	15.15	6.9	9.91	22.57	MgO	1.29	0.44
Impurities					5.71	4.33	Na_2O	0.26	0.14
							NiO	0.21	0.13
							SiO_2	0.90	0.46
							Ta_2O_5	0.05	0.19
							WO_2	0.27	0.49
							ZnO	0.11	0.07

(^{238}Pu-bearing). Three storage temperatures were used: ambient (~20 °C),[1] 125 °C, and 250 °C. These temperatures were selected so that some data would be available for estimating the critical temperature. The specimens were stacked so that the specimens had at least one face that would be a near representation of material far from the surface of the specimen. While the alpha particle and the recoiling atom do not travel great distances in the solid, these particles are lost at a free surface, resulting in a gradient in damage production near the free surface. Alpha particles travel tens of micrometres in solids, while the recoiling atom from alpha decay may travel tens of nanometres. Since the damage effects at a free surface do not represent the damage effects in the bulk of the specimen, the specimens were stacked face-to-face so each surface received uniform damage and became more representative of the bulk.

The specimens were characterized with X-ray diffraction (XRD), dimension measurements, density measurements, and photography. Because the specimens were thin (~2 mm) and highly radioactive and because we needed to control the spread of contamination and reduce the exposure of worker's extremities to radiation, we developed special apparatuses to facilitate the measurement of the dimensions and a specimen holder for obtaining the diffraction patterns from the polished surface of the specimens. Both the dimension measurement device and the specimen holder for XRD are described in detail elsewhere [19,20]. A specimen of Standard Reference Material 1976 (corundum) from the National Institute of Standards and Testing that was permanently affixed to the post of a specimen holder and used to calibrate the intensity and diffraction angles. A diffraction pattern from the standard corundum was obtained at the beginning and end of each day that patterns were being obtained from the test specimens. The XRD unit was a Scintag PAD V (Scintag Corp., Cupertino, CA). The XRD patterns were analyzed with the JADE software (MDI, Livermore, CA).

From the dimension measurements and the mass of the specimen, we could calculate the bulk density. However, a small wobble in the table and edge chips in the specimens prevented us from obtaining precise measurements of the specimen height. So densities were calculated from the specimen diameter and the assumption that the swelling was uniform. Densities were also measured with a helium gas pycnometer (Micromeritics, Norcross, GA, Model AccuPyc 1330). The volume of a weighed specimen(s), including closed porosity, is measured by displacement of He gas. The measurements reported here were obtained with an ultraprecise procedure in which a value for the density is not recorded until five successive determinations agree within 0.05%. For the ^{238}Pu-bearing specimens, three specimens are used in the density determination and two for the ^{239}Pu-bearing specimens.

The dissolution of these materials in water was studied with a single-pass flow-through apparatus described in earlier articles [1,21,22]. In the experiments described here, we used both Teflon® and titanium apparatus to show that the dissolution apparatus did not affect the value of the dissolution rate obtained. Titanium vessels were used when we learned that significant decomposition of the Teflon occurred when the test specimen contained ^{238}Pu [1]. Only the Z1-239 material was used in dissolution testing; budget constraints prevented us from testing the Z1-238 material. We include results from zirconolite-bearing materials that were made with non-radioactive elements to support our conclusions about the dissolution rate of the Pu-bearing materials. Information on the non-radioactive materials can be found in our earlier reports [1,23]. The compositions of these non-radioactive zirconolite-bearing materials was the same as that reported in Table 1, but with Ce taking the place of Pu and U. No other information on these materials is provided here.

At each characterization, the specimens were photographed. This was done to document any visible changes to the specimens with storage time. No visible changes were noted.

In this report, we list the dose in alphas/g (α/g). These are average doses to the entire specimen; we were unable to determine the amount of ^{238}Pu in each phase in the specimen. The dose is calculated from the mass of ^{238}Pu and the half-life of 87.7 y.

At the beginning of the project, we did not have a scanning electron microscope (SEM) in which we could examine specimens containing high concentrations of ^{238}Pu, so no microscopy results are available for the as-made ^{238}Pu-bearing specimens. By the end of the project, we were able to examine these materials. Examinations were performed on a JEOL840 equipped with a Gatan Digital Imaging System, a Robinson Backscattered Detector, and an Oxford ISIS energy-dispersive spectroscopy (EDS) system. A background spectrum collected with the electron beam off was subtracted from all collected spectra; for all specimens containing ^{238}Pu, there is a significant X-ray background from the ^{238}Pu decay product ^{234}U.

3. Results and discussion

In this section, we discuss our results from density measurements, scanning electron microscopic examinations, X-ray diffraction, and dissolution tests. We also provide a photograph of a typical specimen.

3.1. Photographs

A photograph of typical specimens is shown in Fig. 1. The specimens were produced as right circular cylinders. The typical surface flaws and color variations that occur in these specimens are shown in Fig. 1. These surface flaws,

[1] An oven was used but with no power. The oven served as a cabinet to safely house the specimen storage devices. There was sufficient power generated in the specimens to raise the temperature of the 500-g stainless-steel vessel by about 2 °C.

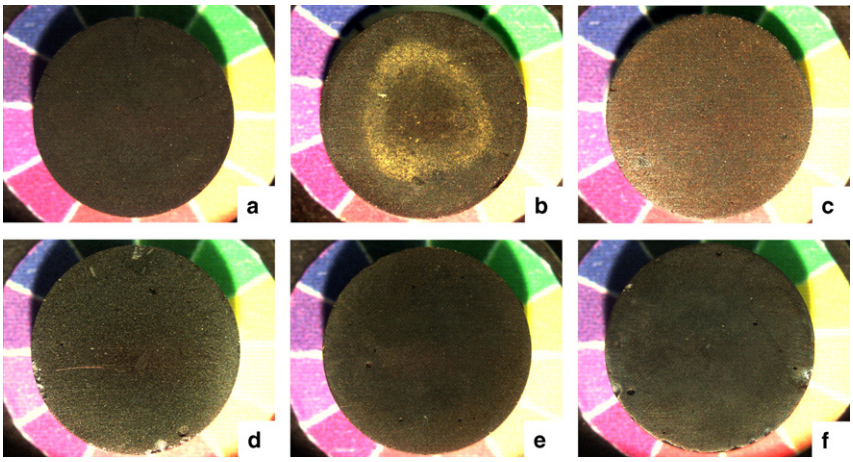

Fig. 1. Pictures of typical, representative Z1 (a, b), ZB1 (c, d), and ZIB1 (e, f) specimens containing ^{238}Pu or ^{239}Pu and stored at 20 °C, 125 °C, or 250 °C.

which presumably occur throughout the bulk of the specimen, result in low measured bulk densities and give rise to spurious peaks in the XRD patterns.

3.2. Density measurements

Here we discuss our results from bulk and 'true' density measurements of the Z1, ZB1, and ZIB1 specimens. From the chemical composition given in Table 1 and an estimate of 3.5 mass% rutile in the Z1 specimens, we calculated the chemical formula for the zirconolite in Z1 as $Ca_{0.86}(Al_{0.10}Gd_{0.05}Hf_{0.93}Pu_{0.13}U_{0.03})Ti_{1.86}O_{7.00}$ based on 7 oxygens or $Ca_{0.86}(Al_{0.10}Gd_{0.05}Hf_{0.79}Pu_{0.13}U_{0.03})(Hf_{0.07}Ti_{0.93})_2O_{7.00}$ based on 2 B-site metals and 7 oxygens. The latter suggests a small B-site occupancy by Hf and is consistent with other studies in which Hf has been found on the B site of a titanate mineral [24–26]. Because we did not have detailed microprobe analyses, we made no attempt to distribute the Pu and U between oxidation states other than four. Several authors have suggested that Pu(III) and U(V) exist in these titanate mineral phases [26–34]. Colella et al. [31] have demonstrated that natural and synthetic brannerite contain U(V) with IR, XPS, and EELS measurements. The natural brannerite samples were X-ray amorphous. Vance et al. [32] have also presented data on U(V) in zirconolites prepared under oxidizing conditions. However, the XAS result reported by Fortner et al. [29,30] for U(V) in pyrochlore ceramics prepared under reducing conditions is probably incorrect. A possible explanation for the observation of Pu(IV) and U(V) in these ceramics may be the accidental analysis of Pu-bearing brannerite, a known U(V) phase, rather than pyrochlore. Only in the study by Fortner et al. [29] is U suggested as occupying the B site; all other results from natural and synthetic pyrochlore or brannerite indicate U mainly on the Ca site. Buck et al. [33] found reduced Pu in synthetic zirconolite for disposition of nuclear weapons Pu that was produced in a reducing environment. With electron energy loss spectroscopy, they also showed that the Ce oxidation state was +3.5 on average, which was consistent with their Pu oxidation state analysis. Begg et al. [34] presented XAS data on Pu(III) and Pu(IV) in zirconolite prepared under oxidizing and reducing conditions.

3.2.1. Helium pycnometer results

3.2.1.1. Z1 specimens. The results of the He pycnometer measurements of the 'true' density of the Z1-238 and Z1-239 specimens are shown in Fig. 2. Although there is a lot of scatter in the data, there should be an insignificant decrease in the density of the ^{239}Pu-bearing specimens. Within the scatter of the data, there appears to be no temperature dependence (dashed line in Fig. 2). For the data from the Z1-238 specimens, two least-squares fits were used. An exponential decay equation (Eq. (1)) was used for the data from the specimens stored at 20 °C and 125 °C. The density results were fit to the equation

$$\rho = \rho_s + b\exp(-ct), \tag{1}$$

where ρ is the density, ρ_s is the density at saturation, b is the difference between the initial and the asymptotic value of ρ, and c is related to the damage volume per alpha decay ([11]). The values[2] are $\rho_s = 4.952(93)\times10^3$ and $5.300(69)\times10^3$ kg/m^3, $b = 0.92\ (11)\times10^3$ and $0.56(7)\times10^3$ kg/m^3, and $c = 0.0023(7)$ and $0.0017(5)$ d^{-1} for the 20 °C and 125 °C data, respectively. 'True' densities from the specimens stored at 250 °C were fit to a straight line. The intercept and slope of the straight line drawn through these data are 5.89×10^3 kg/m^3 and -2.3×10^{-4} kg/(m^3 d), respectively. An extra data point was added to the 125 °C data when the least-squares analysis was performed so that the starting density was the same as the starting density of the 20 °C data. This value, 5.869×10^3 kg/m^3, is similar to the intercept for the linear fit to the 250 °C, 5.89×10^3 kg/m^3. These results also suggest that there is no difference between the specimens that were sintered for 8 h and

[2] The number in () is the standard deviation in the last place of the reported number.

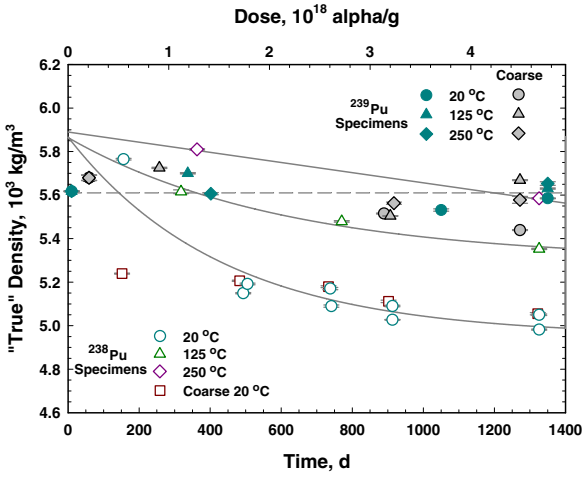

Fig. 2. The change in 'true' density with increasing radiation-induced damage for ^{238}Pu- and ^{239}Pu-bearing Z1 specimens stored at 20 °C, 125 °C, and 250 °C. The solid lines are least squares fits to the ^{238}Pu data and the dashed line is from a linear least squares fit to the ^{239}Pu data.

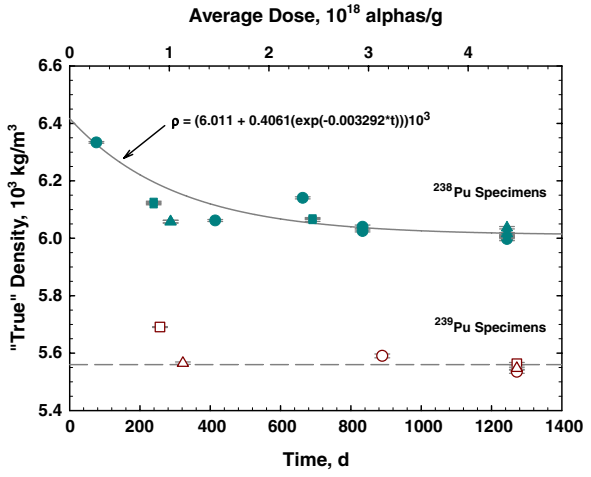

Fig. 3. The change in 'true' density with increasing radiation-induced damage for ^{238}Pu- and ^{239}Pu-bearing ZB1 specimens stored at 20 °C, 125 °C, and 250 °C. The solid line is a least-squares fit to the ^{238}Pu data, and the dashed line is from a linear least-squares fit to the ^{239}Pu data.

those for 100 h (coarsened microstructure). From the extrapolated densities, the change in density from the beginning to saturation is 16% and 9.6% for the 20 °C and 125 °C data, respectively. Since a linear decrease in the density of the specimens held at 250 °C was observed, no fit of these data to Eq. (1) was attempted. The magnitude of the changes in the 'true' densities is likely caused by the increase in closed porosity as the individual grains swell and close access to the He gas to what was open and accessible porosity. This effect is unlikely caused by He bubble formation at the low doses received in these samples; there is no evidence from the SEM analyses (see below). Using the XRD results (see below), we calculate a theoretical density for the Z1 specimens of 5.92×10^3 kg/m^3. Thus, the 'true' densities are 99% of theoretical. According to Shaw [35], when the total porosity in a specimen is about 15% approximately 50% of that porosity is open. For the Z1 specimens, the results for the 'true' density suggest that these specimens have very little closed porosity, implying that the remaining open porosity can be easily converted to closed porosity. This conclusion will be strengthened by the results in the next section where the bulk swelling is incommensurate with the large changes in 'true' density.

3.2.1.2. ZB1 specimens. The results of the He pycnometer measurements of the 'true' density of the ZB1-238 and ZB1-239 specimens are shown in Fig. 3. Results from the measurements of the 'true' densities of the ZB1-239 specimens were averaged, leaving out the high value, to get an average density of 5.560×10^3 kg/m^3 (dashed line in Fig. 3). For the ^{238}Pu-bearing specimens, no temperature dependence was noted (Fig. 3). Therefore, all the data were least squares fit to Eq. (1). The values are $\rho_0 = 6.01(4) \times 10^3$ kg/m^3, $b = 0.41(8) \times 10^3$ kg/m^3, and $c = 0.0033(18)$ d^{-1} (Fig. 3). The 'true' densities decrease by 6.3% for the ZB1-238 specimens. The magnitude of the density change suggests an increase in the closed porosity at the expense of open and accessible porosity (see below).

3.2.1.3. ZIB1 specimens. When performing the least-squares analysis for the 'true' densities of the ZIB1-238 specimens (Fig. 4), we added the data point at zero time that was the same as the ^{239}Pu-bearing ceramics. The validity of this approach could be questioned, but, with the paucity of data, we considered this to be the only real choice when analyzing the data. Although the lines shown in Fig. 4 are from a least-squares fit of the data to Eq. (1), we do not report the values here because of the lack of sufficient data to support any conclusions from such a fit. Rather, we show the lines as a guide to the eye. As with the ZB1-238 specimens, there does not appear to be a significant dependence on the storage temperature. Apparent

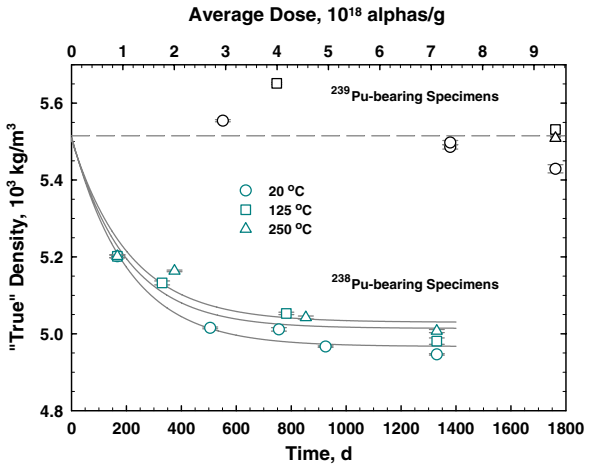

Fig. 4. A graph showing the change in the 'true' density for the ^{238}Pu- and ^{239}Pu-bearing ZIB1 specimens.

changes in the density of the ZIB1-238 specimens are −9.9%, −9.0%, and −8.6% for specimens stored at 20 °C, 125 °C, and 250 °C, respectively. However, the data do not support a dependence on storage temperature. Hence, an average value of 9.2% decrease should be used.

3.2.2. Geometric densities

As seen in the picture of a typical specimen (Fig. 1), there are chips on the edges of the specimens. This, combined with a 20-μm wobble in the table on which the specimen rested during the measurement, caused a significant variation in the measured height of the specimen and a concomitant uncertainty in the calculated geometric density of the specimen. Therefore, as a measure of the change in the geometric density, we consider changes in diameter of the specimen with increasing dose.

3.2.2.1. Z1 specimens. The change in diameter with time (dose) for the Z1-238 and Z1-239 specimens is shown in Fig. 5. Here the diameters of all the specimens stored at all temperatures are shown. There is no discernable difference between specimens stored at any temperature. The initial (day zero) measurement of the diameter was done with a hand-held micrometer. This value 10.94(6) mm is an average of 25 specimens and agrees well with the extrapolated value of 10.88(4) mm from a linear fit of the diameter measurements between 338 and 924 days. Using a value of 11.13 mm for the saturation value for the specimen diameters and the starting value of 10.94 mm, we calculate a 1.7% increase in the diameter from radiation-induced swelling or a 5.0% decrease in the density of the specimens when approximately 5×10^{18} α/g have accumulated. No change was expected from radiation-induced swelling in the diameter of the Z1-239 specimens. This decrease and lack of dependence on storage temperature in the geometric density of the ^{238}Pu-bearing specimens is inconsistent with the 'true' density changes discussed above but consistent with the conversion of open to closed porosity with radiation-induced swelling. The initial densities of the Z1-238 and Z1-239 specimens were $5.17(2) \times 10^3$ kg/m^3 and $4.75(2) \times 10^3$ kg/m^3 or 87% and 80% of theoretical density, respectively. Since about half of the porosity is open, a rapid decrease in the 'true' density of the Z1-238 specimens relative to the changes in the geometric density are possible.

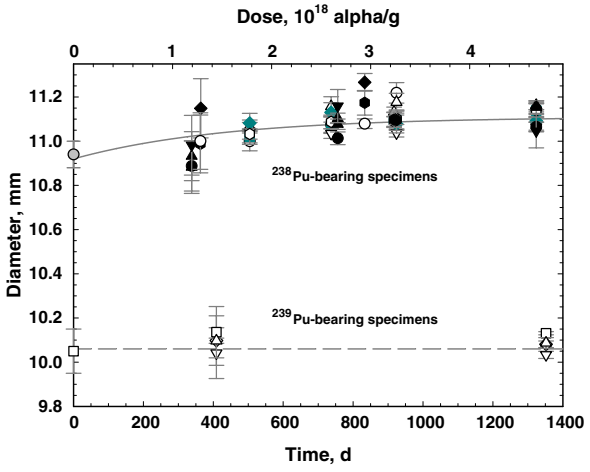

Fig. 5. The change in the density of all Z1 specimens with increasing alpha dose.

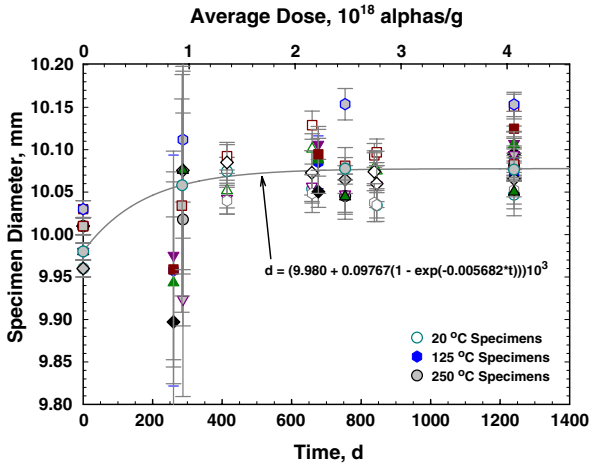

Fig. 6. The change in the diameter of all ^{238}Pu-bearing ZB1 specimens with increasing alpha dose.

3.2.2.2. ZB1 specimens. The change in the diameters of the ZB1-238 and ZB1-239 specimens with increasing dose at all temperatures is shown in Fig. 6. Like the 'true' density changes for these specimens, there is no discernable difference between specimens stored at any temperature. The initial (day zero) measurement of the diameter 9.98 mm was done with a hand-held micrometer. The majority of the ^{238}Pu-bearing specimen data were fit to the following equation:

$$d = d_0 + a(1 - \exp(-bt)), \tag{2}$$

where d is the specimen diameter, d_0 is the diameter at zero dose (mm), a is the difference between the initial and the asymptotic (saturation) value of d (mm), and b (d^{-1}) is related to the damage volume per alpha decay [11] and the half-life of the active isotope. Using the asymptotic value for the diameter of 10.08 mm, we calculate a 0.98% increase from radiation-induced swelling or a 2.9% decrease in the density of the specimens when approximately 3×10^{18} α/g have accumulated (900 days). This decrease in the geometric density is inconsistent with the 'true' density changes discussed above but consistent with the conversion of some open and accessible porosity to closed porosity as the specimen swelled.

3.2.2.3. ZIB1 specimens. For the ZIB1-238 and ZIB1-239 specimens, the variation in the specimen diameters is shown in Fig. 7. A handheld micrometer was used to measure the starting diameters of the ZIB1-238 specimens, which averaged 10.30(1) mm. The diameters of the

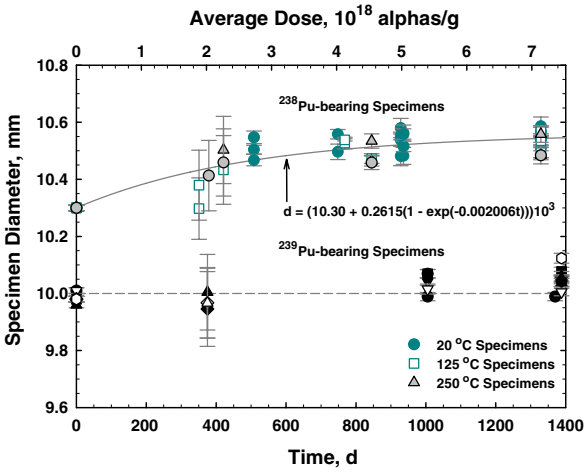

Fig. 7. The variation in the diameters of the ^{238}Pu- and ^{239}Pu-bearing ZIB1 ceramic specimens.

ZIB1-239 specimens averaged 9.98(1) mm. We then fit the diameters of the ZIB1-238 specimens to Eq. (2) to obtain the values for the parameters of $d_0 = 10.30(1)$ mm, $a = 0.26(3)$ mm, and $b = 0.0020(5)$ d^{-1}. More significant figures are given in Fig. 7 to allow the reader to more accurately reproduce the fit to our data. This treatment of the data yields a value for the swelling of these specimens of 2.5%. From this swelling, we calculate a 7.1% decrease in the bulk density of these specimens. Saturation of the bulk swelling occurs after about 6.5×10^{18} α/g have accumulated. The average change in the 'true' density was −9.2% for these specimens stored at all temperatures. As determined for other specimens in this study, some open porosity was likely converted to closed porosity with increasing radiation-induced swelling. As with the 'true' densities of these specimens, no dependence on the storage temperature was noted.

3.3. Scanning electron microscopy

In this Section, we discuss the results from our SEM examination of Z1-238, Z1-239, ZB1-238, and ZB1-239 specimens. No SEM analyses were made of the ZIB1 specimens.

3.3.1. Z1 specimens

Results from the examination of the original Z1-238 (fully damaged) and Z1-239 specimens that were stored at 20 °C are shown in Figs. 8 and 9. The secondary electron image shows the pores in the material (Fig. 8(a)), whereas the backscattered electron image shows the difference in average atomic number more clearly (Fig. 8(b)). By combining the back-scattered electron and secondary electron images, both the contrast (effective atomic number) and the surface defects can be observed (Fig. 8(c)). Although not clear in these black and white photomicrographs in Fig. 8(c), there are subtle contrast variations in the zirconolite phase, suggestive of variations in composition. These variations were initially interpreted as coming from the presence of a pyrochlore phase. However as discussed later, the XRD results are consistent with the presence of

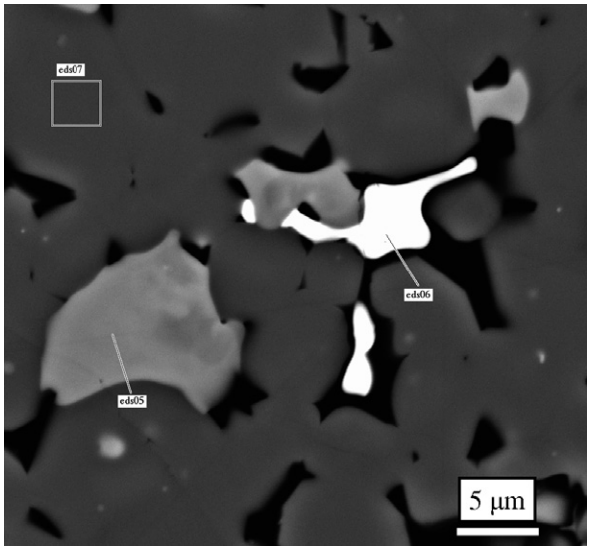

Fig. 9. Photomicrograph of a Z1-239 specimen: (a) low resolution image showing the overall microstructure, and (b) a higher magnification showing the distribution of phases.

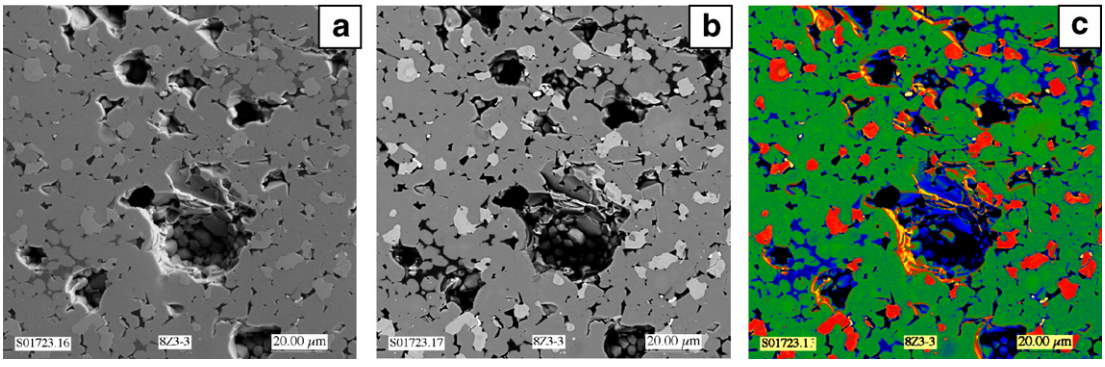

Fig. 8. Photomicrographs of a Z1-238 specimen (stored at 20 °C; fully damaged): (a) secondary electron image, (b) backscattered electron image, and (c) combined images A and B (grey = zirconolite; medium grey = brannerite; medium-dark grey = porosity; and black = rutile).

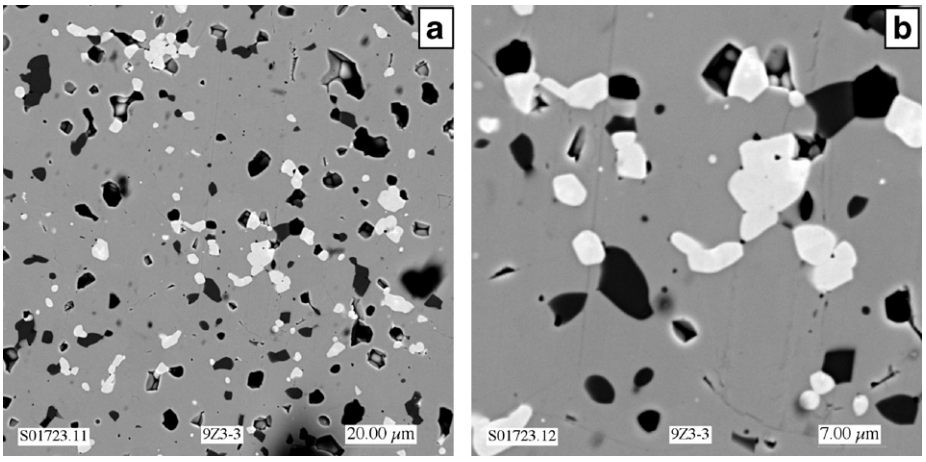

Fig. 10. Backscattered electron image of a ZB1-238 specimen stored at 20 °C; fully damaged: low (a) and high (b) magnification showing three major phases. The dark contrast may be due to pores in the ceramic.

zirconolite and no pyrochlore. These contrast variations are likely the result of electron channeling and other effects caused by the changes in physical properties from the radiation-induced damage of the zirconolite phase. This interpretation is supported by recent work by Nasdala et al. [36].

There were differences between the ^{238}Pu and ^{239}Pu ceramic microstructures. In particular, the distribution of rutile in the Z1-238 was intergranular (Fig. 9), whereas the rutile tended to occur as discrete grains within the Z1-239. Fig. 10 shows the lower magnification image of the Z1-239 specimen that does not exhibit as much porosity, although this may be a localized case since the densities of the Z1-238 are greater than the densities of the Z1-239 specimens. In Fig. 11, the SEM image shows a concentric–spherulitic grain in Z1-238 that possesses multiple shells with different contrast. The particle consists of three different compositions based on backscattered electron contrast. It is unlikely that this effect is from thickness variations; the sequence of light, darker, lighter indicates that this is an actual compositional profile or radiation-induced damage effects [36]. Actinide oxide inclusions are observed within the pyrochlore grains. The inclusions associated with the rutile (black contrast) are from srilankite-like composition ($HfTiO_4$).

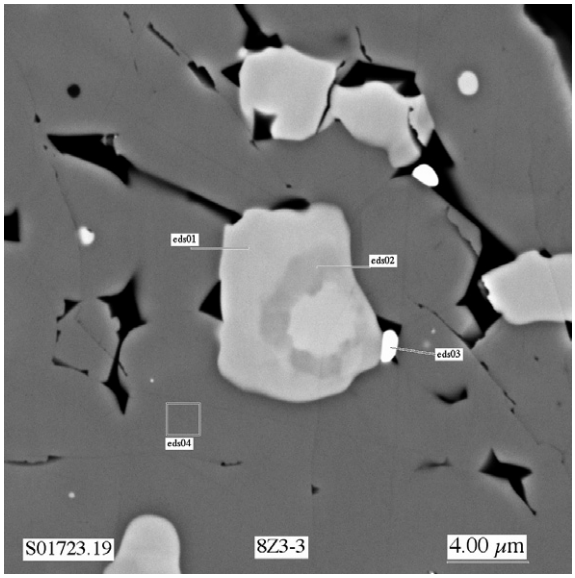

Fig. 11. Higher magnification images of region highlighted in Fig. 8.

In Fig. 9, rutile appears as the darkest in the Z1-238 specimen and occurs as anhedral precipitates in the surrounding other grains. This indicates that this phase formed after the zirconolite. Compared to the Z1-239 specimen, the distribution of rutile is quite different. In some instances, the rutile itself appears to have undergone exsolution, resulting in the precipitation of a Hf-titanate (the phase colored white within the black in Fig. 9). This phase may be a Hf-srilankite ($Hf_{1-x}Ti_xO_4$) related structure. Zirconium titanate ceramics similar to those observed in this study have been produced by solid-state reaction of ZrO_2 and TiO_2. By reacting in the presence of transition-metal oxides and rare-earth oxides, the formation temperature can be lowered to around 1100 °C. Kong et al. [37] have reported solid solutions of $(Zr_{1-x}Ti_x)O_2$ ($x = 0.44$, 0.48, 0.52 and 0.60) with a srilankite structure that were produced with ball-milling and sintering powders of ZrO_2 and TiO_2. Natural srilankite is sometimes reported as $ZrTi_2O_6$. In Table 2, the backscattered contrast factors have been calculated based on the srilankite ($ZrTiO_4$) unit cell. The average Z contrast for a Hf-srilankite would be predicted to be similar to a Pu-bearing pyrochlore. This illustrates that backscattered electron contrast can be deceptive for estimating actinide content.

3.3.2. ZB1 specimens

Two major phases were observed in a sample of the original (fully damaged) ZB1-238 specimen that was stored at 20 °C: zirconolite (dark gray veins) and pyrochlore (lighter grey material) (Fig. 12). A minor $HfTiO_4$ (Hf-srilankite)

Table 2
Plutonium titanate ceramic compositions with an estimation of the backscattered contrast factor

	Al	Ca	Gd	Hf	U	Pu	Ti	Metal	Average Z[a]	Molecular weight	Density, 10^3 kg/m^3	Oxygens per unit	Units per cell
Pyrochlore[b]	0.10	0.85	0.22	0.27	0.44	0.22	1.90	4.00	49.76	479.80	7.14	7	10
Zirconolite[b]	0.28	0.72	0.15	0.80	0.16	0.12	1.77	4.00	45.95	466.29	7.78	7	10
Brannerite	0.05	0.06	0.10	0.12	0.53	0.24	1.90	3.00	54.40	411.41	5.98	6	2
Hf-Rutile	0.01	0.00	0.00	0.09	0.01	0.00	0.89	1.00	27.56	93.35	4.96	2	2
$HfTiO_4$	0.00	0.00	0.00	1.00	0.00	0.00	1.00	2.00	49.65	290.40	7.30	4	2

Density (calculated) = [Average weight] · ([Form.units per cell])/([volume] × 0.60225) where the atomic weight is in g/mol, the volume in m^3, and 0.60225 is the Avogadro constant.

[a] The average Z (mass fraction) provides a guideline for the expected backscattered contrast on the pyrochlore/zirconolite ceramic phases. Brannerite should appear the brightest and rutile the darkest phase in the backscattered electron images. The $HfTiO_4$ phase, although it contains no actinides, would also exhibit high Z contrast.

[b] The compositions of the zirconolite and pyrochlore phases have been estimated and are not the same as those observed in this study.

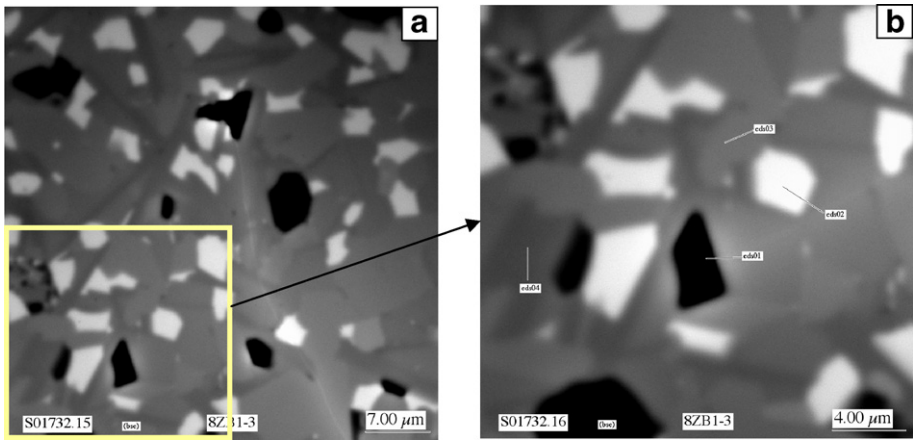

Fig. 12. Backscattered electron image of a ZB1-238 specimen stored at 20 °C; fully damaged: low (a) and high (b) magnification showing three major phases. The dark contrast may be due to pores in the ceramic.

phase was also present (white contrast in Fig. 12(a)). The microstructure of the ZB1-238 cannot be easily seen in Fig. 12(b) because of SEM sample preparation problems. However, zirconolite veins can be seen as dark bands within the more abundant grey. These features were much more clearly visible in the ZB1-239 specimen (see Fig. 13(a) and (b)).

The ZB1-239 specimen also exhibited two main phases, zirconolite and pyrochlore (Fig. 13(a) and (b)), similar to the ZB1-238 specimen. Veins of euhedral zirconolite crystals are clearly visible running through the pyrochlore in Fig. 13(b). This suggests that the pyrochlore solidified after the zirconolite phase. The evidence from the photomicrographs suggests that as the pyrochlore crystallized, Pu-rich

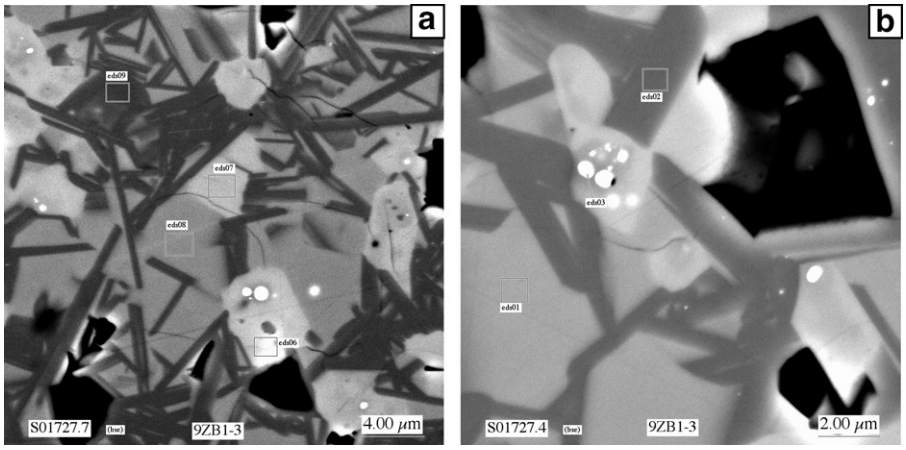

Fig. 13. Photomicrographs of a ZB1-239 specimen: (a) distribution of phases, and (b) high actinide inclusions.

phases (from the excess Pu) precipitated as inclusions. These inclusions were not observed in the zirconolite crystals. This indicates that the pyrochlore became increasingly more concentrated in Pu as the specimen cooled until Pu saturation, then Pu inclusions form (Fig. 13).

3.4. X-ray diffraction

3.4.1. Z1 specimens

Results from the analyses of the XRD patterns from the Z1 specimens indicated that the material was essentially phase pure with low amounts of $HfTiO_4$. Fig. 14 shows the results from the XRD analysis of the Z1-238 and Z1-239 specimen. The diffraction peaks from the Z1-238 specimen align with those from the Z1-239 specimen with slight changes from the effects of radiation-induced damage. These results suggest that the SEM analysis is consistent with a slight variation in the composition of the zirconolite phase rather than pervasive pyrochlore. If the variations noted in the SEM are the result of compositional variations, then the SEM and XRD data suggest that there are subtle stability relationships that have not been investigated in previous studies. It is more likely, that the apparent variations in composition are an artifact of the SEM analyses. Also suggested by the XRD patterns and consistent with the SEM results is that $HfTiO_4$ is a minor component. In previous sections, we report the theoretical density of the Z1-239 specimen. This is based on the lattice parameters (nm) for zirconolite of $a = 1.24568$, $b = 0.72619$, $c = 1.13537$, and $\beta = 100.656°$ and for Hf-rutile $a = 0.4631$ and $c = 0.2972$. Because we did not have good results from the SEM on the amount of Hf in $HfTiO_4$, it was assumed to have the same Hf/Ti as the Hf-rutile, namely 0.25. This assumption leads to theoretical densities for the two phases that are about equal. The estimate of the theoretical density of the specimens is not a sensitive function of the composition or the amounts of the rutile or $HfTiO_4$ phases because these elements are taken from the zirconolite phase, the composition of which is more sensitive to the composition and amount of the minor phase(s).

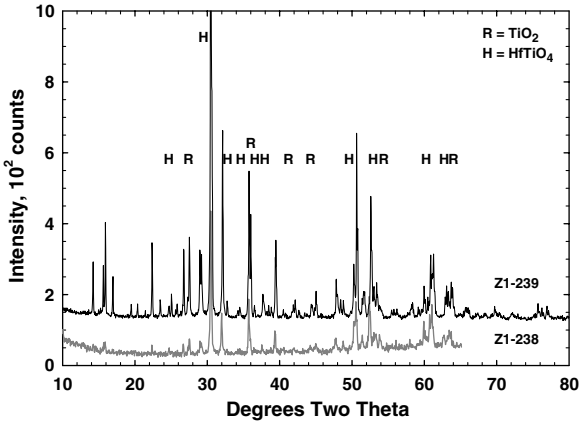

Fig. 14. A comparison of the XRD patterns from Z1-238 and Z1-239 specimens. Only rutile (R) and $HfTiO_4$ diffraction peak locations are shown, but do not contribute to all the intensity of all the peaks.

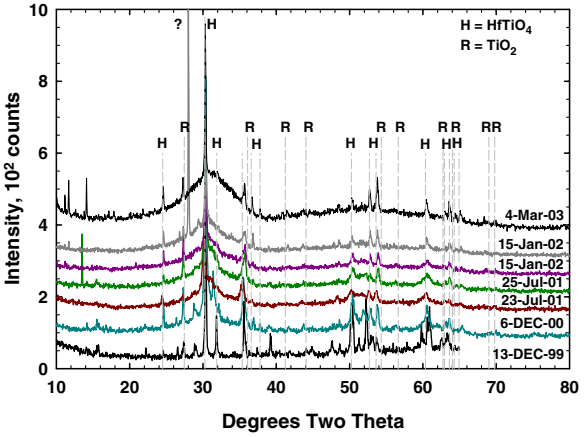

Fig. 15. A summary of the XRD patterns from the ZB1-238 specimens. Only the diffraction peaks from phases other than zirconolite are marked. The sharp peak in the 15-Jan-02 pattern marked with a '?' comes from a pellet surface defect.

The evolution of the XRD pattern from the Z1-238 specimen with time (dose) is shown in Fig. 15. Although we track the changes in the XRD patterns with time (dose), we recognize that at some point, it is not possible to distinguish Bragg diffraction associated with the phase undergoing radiation-induced damage and the diffuse scattering that results from that damage [38,39]. It is outside the scope of this study and our data are of insufficient quality to attempt to separate these parameters. Recognizing these difficulties, we continue the XRD analyses to provide a comparison to past work in this field.

As noted by Wald and Offerman [40] and Strachan et al. [41], the expansion of the zirconolite monoclinic cell occurs predominantly along the c-axis with increasing radiation-induced damage. This is most noticeable with the (004) [hkl] diffraction peak that occurs at 31° 2θ, which shifts to lower 2θ with increasing dose (Fig. 15). By July 2001, this diffraction peak has become a broad shoulder on the side of a growing broad maximum (from the amorphous material) beneath the main zirconolite and $HfTiO_4$ diffraction peak (Fig. 15). With increasing radiation-induced damage, the contribution of the $HfTiO_4$ phase to the strong diffraction peak at approximately 30° 2θ becomes more significant so that by March 2003 it is the sole contributor to the sharp peak at this diffraction angle.

Illustrated in Fig. 14 are the XRD patterns from the first Z1-238 specimen in December 1999 (also shown in Fig. 15) and a ^{239}Pu-bearing specimen from March 2000. A significant amount of degradation of the diffraction pattern has occurred over the 153 days since the ^{238}Pu-bearing specimen was made (13-July-1999); many of the less-intense peaks have become indistinguishable from background, and some have broadened noticeably. By 741 days (23-July-2001, 2.6×10^{18} α/g), the zirconolite had become X-ray amorphous (Fig. 15). Insufficient XRD patterns with a sufficient number of diffraction peaks were available for

us to determine the change in lattice parameters with increasing dose. However, the lattice parameters for the zirconolite in Z1-239 are, in nm, $a_0 = 1.24566(12)$; $b_0 = 0.72621(6)$; $c_0 = 1.13535(12)$; $\beta = 100.656(7)°$, volume $= 0.1281(72)$ nm^3 and from the Z1-238 specimen $a_0 = 1.25081(35)$; $b_0 = 0.72671(21)$; $c_0 = 1.14276(36)$; $\beta = 100.714(20)°$, volume $= 0.1891(206)$ nm^3. It should be noted that the ^{238}Pu-bearing specimen had accumulated 5.4×10^{17} α/g, a significant fraction of the dose needed to make the zirconolite X-ray amorphous. Therefore, a slightly larger unit cell with the dimensions having higher uncertainties was expected because of the accumulated dose and the less well defined diffraction peaks.

Unlike the pyrochlore dominated specimens discussed in Strachan et al. [1], these specimens showed no indication of phase transitions from the radiation-induced damage accumulation when stored at elevated temperatures. We did not sinter any specimens that had become amorphous from damage accumulation.

Although we did not obtain many XRD patterns over the time span during which most of the damage occurred, we saw no evidence for a transition from zirconolite to pyrochlore to fluorite before the specimens became X-ray amorphous. Disordered fluorite is reported as a phase through which these titanates transition before becoming amorphous [14]. Evidence for the in-growth of pyrochlore would have led to the appearance of the characteristic (3 1 1) pyrochlore diffraction peak at 28–29° 2θ. As the zirconolite peaks became broader and less intense, the diffraction from TiO_2 and $HfTiO_4$ became relatively more intense (Fig. 15) because these phases contain no ^{238}Pu.

From the broad maxima that remain in the XRD pattern after the zirconolite in the Z1-238 specimen has become amorphous, we obtained estimates of the metal–oxygen and metal–metal distances in the fully damaged material. These were obtained through the use of the JADE program (MDI, Livermore, CA) after removing the background. The values that were determined are 0.177(2) nm (M–O) and 0.288(3) nm (M–M).

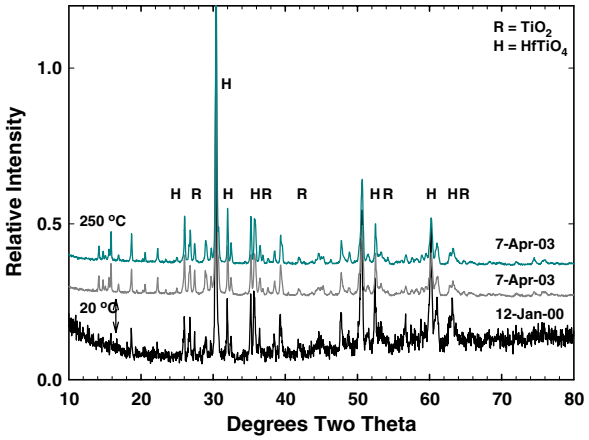

Fig. 16. A comparison of the XRD patterns of the ZB1-239 specimen from early in the study and at the end at 20 °C and 250 °C. Only rutile (R) and $HfTiO_4$ (H) peak locations are shown, but do not constitute all the intensity for the peak located at this diffraction angle.

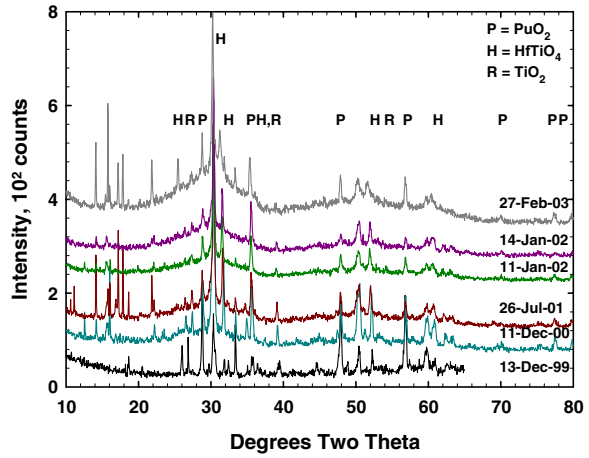

Fig. 17. A summary of the XRD patterns from the ZB1-238 specimens. Only the PuO_2 (*P*), $HfTiO_4$ (H), and rutile (R) diffraction peaks are marked, but these phases do not contribute all of the intensity to all of the peaks at these diffraction angles.

3.4.2. ZB1 specimens

Results from the analyses of the XRD patterns from the ZB1-239 specimens indicated that the material was composed predominantly of zirconolite, pyrochlore, and brannerite (Fig. 16). This phase assemblage did not change over the course of 1700 days, nor was there any change in the phase assemblage at elevated temperatures. Over those 1700 days, we improved at obtaining the patterns, and we obtained a dedicated XRD unit, both of which explain the better signal-to-noise in the later patterns. The evolution of the XRD pattern with time (dose) for the ZB1-238 specimen is shown in Fig. 17. The dose accumulated in this specimen was 4.4×10^{18} α/g over 1246 days. There is an additional phase in the ZB1-238 specimen, namely PuO_2 (Fig. 17). This excess PuO_2 appeared to have precipitated from the pyrochlore as the specimen cooled and remained as an additional phase in the ceramic (see the SEM results above). Plutonium oxide is not significantly affected by radiation-induced damage [42]. Brannerite appears to have undergone significant radiation-induced damage because only a few diffraction peaks attributable to brannerite remain in the diffraction pattern. After an additional year of accumulated dose, the brannerite diffraction peaks largely disappeared.

Of note is the presence of preferred crystal orientation in some of the patterns. Some of the specimens have pits that occur on the surface (Fig. 1), and these could also cause diffraction to occur at angles different than the majority of the specimen that is in proper alignment. Because these pits are not always in the same orientation when the specimen is remounted, the peaks do not always occur or occur with the same intensity. Fortunately, these errant diffraction peaks do not interfere with the overall interpretation of the diffraction pattern. The phase that survives the

longest, possibly because it contains less ^{238}Pu than the pyrochlore, is zirconolite. The last diffraction pattern shows the presence of $HfTiO_4$, which has an orthorhombic unit cell, zirconolite, and PuO_2 (Fig. 17).

As noted above in the discussion of the Z1-238 specimens, the expansion of the zirconolite monoclinic cell occurs predominantly along the *c*-axis with increasing radiation-induced damage. This is most noticeable with the (0 0 4) diffraction peak that occurs at 31° 2θ, which shifts to lower 2θ (Fig. 17). Zirconolite does not transform to pyrochlore as suggested by Wang et al. [14], since there is no characteristic (3 1 1) peak on the low 2θ side of the main diffraction peak. Zirconolite appears to transform from the monoclinic cell to an amorphous phase as shown by the peaks between 50° and 54° 2θ that change in relative intensity, but in a manner inconsistent with the ingrowth of a pyrochlore or fluorite phase (compare the patterns from the ^{239}Pu-bearing and ^{238}Pu-bearing specimens) shown in Figs. 16 and 17, respectively.

3.4.3. ZIB1 specimens

The ZIB1-239 specimen is composed of zirconolite, pyrochlore, brannerite, and rutile and shown in the diffraction patterns from the specimens (Fig. 18). This figure shows that the phase character of the specimens did not change in over 1390 days of storage, irrespective of storage temperature. Diffraction patterns from the ZIB1-238 specimen (Fig. 19) showed that the brannerite phase was amorphous before the first pattern was obtained at 165 days after it was made (0.9×10^{18} α/g). As reported in previous sections, it appears that brannerite readily becomes amorphous with small amounts of radiation-induced damage. This is consistent with the thermodynamic instability of brannerite [43]. In the ZIB1-238 specimen, there does not appear to be any significant rutile since there are no diffraction peaks of significance in the last pattern obtained in 2003 (Fig. 12). The zirconolite phase remains identifiable in all but the last pattern taken. Remnants of the main

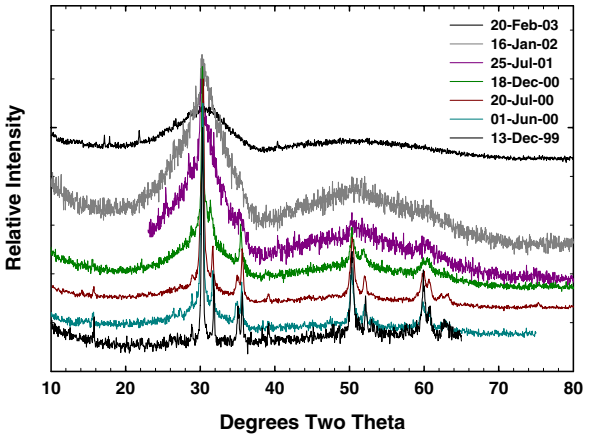

Fig. 19. A comparison of the XRD patterns from ZIB1-238 specimens (the order of the patterns is the same as the order in the legend).

peaks can still be seen in the last pattern taken in 2002 after 960 days during which time about 5×10^{18} α/g were accumulated. In Fig. 20, we show in more detail the zirconolite diffraction maxima and the persistence of the pyrochlore (3 1 1) diffraction peak.

3.5. Dissolution

As indicated above, we performed dissolution experiments with Z1-239 specimens and with specimens that had a similar composition, but with Ce replacing Pu and U. Concentrations of Ca, Ce, Gd, and Ti from the non-radioactive zirconolite specimens for experiments performed at a pH of 2 and 90 °C exhibited steady-state concentrations after 200 days. In higher pH solutions (7–10), dissolution rates were monitored by the release of Mo because concentrations of Ce, Gd, and Ti were likely solubility limited. A lack of the dependence of the dissolution rate on pH is shown in Fig. 21 in which the Mo concentrations are shown for leachants with pH values from 7 to 10.

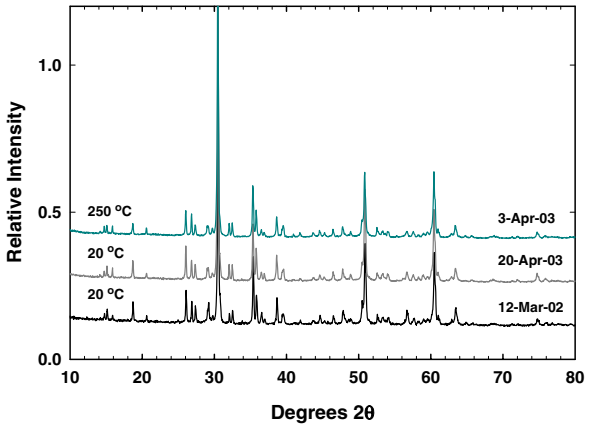

Fig. 18. A comparison of the XRD patterns from the ZIB1-239 specimen from early and at the end of the study for 20 °C and 250 °C, showing the stability of the phase assemblage over long time at elevated temperature.

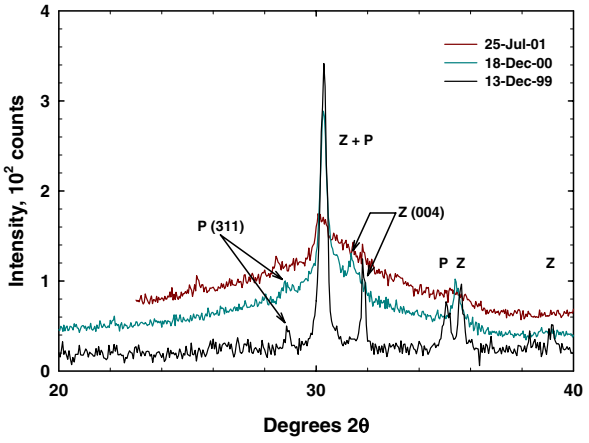

Fig. 20. A detail of the three XRD patterns from Fig. 18 showing the changes in the zirconolite and pyrochlore phases in the ZIB1-238 specimen (the order of the patterns is the same as in the legend).

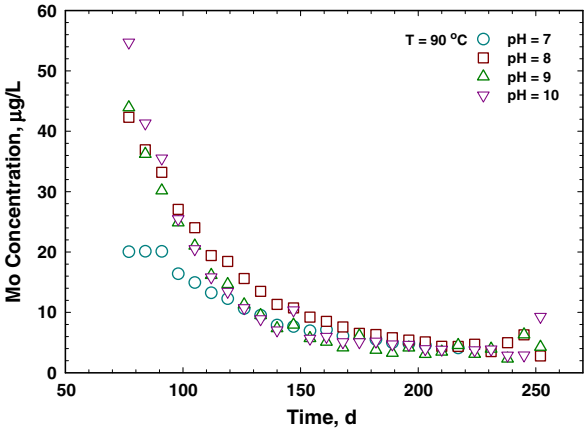

Fig. 21. A graph of Mo concentrations from the single-pass flow-through test with time for the non-radioactive zirconolite specimens at various pH values.

At lower pH values, we used Ce and Ca as the indicators of dissolution because of the sorption of Mo on anatase [44], a common alteration product of these ceramics. At pH values from 7 to 2, the dissolution rates do not change much [45]. There is no more than a factor of ten variation in the dissolution rate as a function of pH with the minimum dissolution rate occurring at approximately 7.

Results from the SPFT tests on Z1-239 are summarized along with the results from the experiments on the non-radioactive specimens in Fig. 22. As we noted in our earlier article [1], it is important that one establishes the dissolution rate of a material under experimental conditions where the dissolution rate is independent of flow rate (q, m^3/s) or flow rate divided by the surface area (S, m^2). For these materials, the dissolution rate is independent of q/S (m/s) at values of $\log_{10}(q/S) > -8$. Although our radioactive sample experimental conditions were at values of $\log_{10}(q/S) < -8$, we have shown that these results, when taken in the context of the results from the non-radioactive specimens, yield valid information on the dissolution rate of zirconolite [1]. Thus, the dissolution rate for the Z1

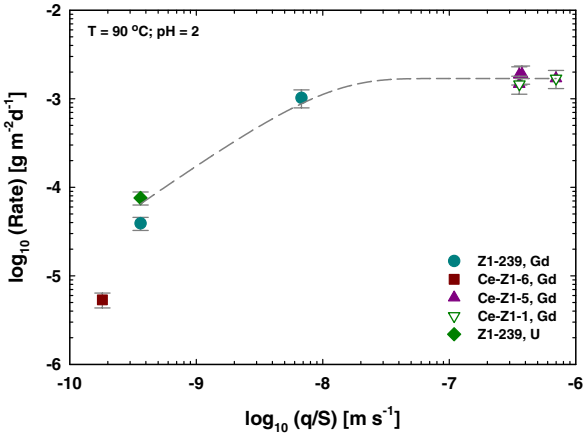

Fig. 22. A plot of $\log_{10}$ (rate) [g/(m^2 d)] versus $\log_{10}$(q/S) (m/s) at 90 °C and pH 2 for the non-radioactive and Z1-239 specimens in this study.

material is $1.7(4) \times 10^{-3}$ g/(m^2 d). Since the Z1-239 specimens were tested in both the Teflon and the titanium reactors, our results provide evidence that the rates do not depend on which of these two materials were used to construct the dissolution apparatus: the difference in rate between the two specimens can be interpreted as a consequence of the faster flow rate in the titanium reactor. It is also significant that the Z1-239 specimen that was tested in the titanium reactor dissolves at the forward rate. Since the Z1-239 material dissolves a the same forward rate as the non-radioactive materials and the entire data set is consistent (low to high q/S and the presence of Ce or Pu and U), the rate of dissolution is invariant with not only reactor type, but Pu-loading as well.

In our earlier paper, we presented results on the dissolution of pyrochlore and pyrochlore-bearing ceramics [1]. The dissolution rates (forward rate) for these materials were 3.9×10^{-3} and 7.2×10^{-3} g/(m^2 d), respectively. These compare with the value reported here for the zirconolite-bearing ceramic (Z1) of 1.7×10^{-3} g/(m^2 d). Given the uncertainties in the data, there probably is not a large dependence on composition.

Both pyrochlore [1] and zirconolite dominated specimens showed dissolution rates that were independent of the amount of radiation damage. In our SPFT experiments, we have attempted to remove the unconstrained variable of solution composition by performing these tests at q/S values that yield constant dissolution rates. The dissolution rate for ^{238}Pu-bearing specimens that had received internal doses that far exceeded those needed to make the material X-ray amorphous were the same within experimental error before and immediately (<3d) after extensive sintering to remove the accumulated damage. These dissolution rates compare well with the specimens that contained no Pu and with those that contained ^{239}Pu. The fact that the dissolution rates for the amorphous and crystalline materials are the same suggests at least two possibilities. The first is that there is no dependence on the amorphous state and the second is that the dissolution in these experiments is dictated by a very small amount of alteration product that is the same for both amorphous and crystalline forms. The latter is possible for an alteration product that is very insoluble; so insoluble that even with very high q/S values its presence controls the dissolution rate. The insoluble product on the surface could control the dissolution rate through some as yet to be determined rate limiting solution species. In static or low q/S tests, however, the radiolysis of the surrounding solution can affect the dissolution kinetics. Our point here is that radiolysis of the solution is tantamount to an unconstrained variable, i.e., the solution composition is unknown. Therefore, removing the radiolysis question by performing SPFT experiments at high q/S values leads to a better constrained experiment with the outcome that there is no measurable difference between Pu-bearing pyrochlores or zirconolites and their states of crystallinity.

4. Conclusions

Radiation-induced damage effects on the crystal structure, dimensions, and density have been measured for multiphase ceramics in which zirconolite is the dominant phase. Specimens were prepared with ^{239}Pu (Z1-239, ZB1-239, and ZIB1-239) that were used as references for the changes that occur from self-irradiation from ^{238}Pu (Z1-238, ZB1-238, and ZIB1-238). The dissolution rate of the Z1-239 material was also determined. From the chemical composition given in Table 1 and an estimate of 3.5 mass% rutile, we calculated the chemical formula for the zirconolite in Z1 as $Ca_{0.86}(Al_{0.10}Gd_{0.05}Hf_{0.93}Pu_{0.13}U_{0.03})Ti_{1.86}O_{7.00}$ based on 7 oxygens or $Ca_{0.86}(Al_{0.10}Gd_{0.05}Hf_{0.79}Pu_{0.13}U_{0.03})(Hf_{0.07}Ti_{0.93})_2O_{7.00}$ based on 2 B-site metals and 7 oxygens. No attempt was made to distribute the Pu and U to different oxidation states; only Pu(IV) and U(IV) were used. Also assumed in this calculation is that the formula for the rutile was $(Hf_{0.2}Ti_{0.8})O_2$. With these formulae and the XRD results, we calculated a theoretical density for these specimens of 5.92×10^3 kg/m^3. Although the XRD results showed that there were two Hf–Ti phases present, we assumed that these phases were Hf-rutile ($Hf_xTi_{1-x}O_2$) when calculating the chemical formula for zirconolite in the Z1 specimen. The two Hf–Ti phases were Hf-rutile and $HfTiO_4$, which can have a variable Hf/Ti [37]. There was a rapid decrease in the 'true' density of the Z1-238 specimens stored at 20 °C between 0 and about 500 days. The 'true' density data from 20 °C and 125 °C indicates that the 'true' density decreases by 16% and 9.6%, respectively. There were insufficient data to make a similar determination for the 'true' density of the specimens stored at 250 °C. The radiation-induced swelling of the diameters of the Z1-238 specimens was 1.7% or a calculated bulk density decrease of 5.0%. We conclude, as we did for the pyrochlore materials in our study [1], that the differences between the changes in the 'true' densities and the bulk swelling estimates (based on changes in specimen diameters) come from changes in open porosity in the 'true' density measurements. Open porosity was converted to closed porosity as individual grains of the specimen swelled in response to radiation-induced damage. The XRD patterns show that the specimens consist of zirconolite, $HfTiO_4$, and TiO_2. There is a progressive loss of intensity and a general broadening of the diffraction peaks before the zirconolite becomes amorphous. There is no evidence for a progression from zirconolite to pyrochlore to fluorite before the material becomes amorphous. This is consistent with the conclusions of Lumpkin et al. [46] and different than what is reported by others [14,15,47]. By 740 days (2.6×10^{18} α/g), the zirconolite is X-ray amorphous. This is well before the time at which radiation-induced swelling saturates, 900 days (3.2×10^{18} α/g), a time equivalent to nearly 700 years of α-dose from ^{239}Pu in a repository.

For the Z1-238 specimen, the major phases identified with SEM included zirconolite, brannerite, and rutile. In these ceramics, zirconolite is a dominant phase, and the characteristic elongated crystal growth was absent. This may allow the ceramic to become amorphous more rapidly; however, EDS analyses appeared to indicate that the Pu content in the zirconolite was relatively low in comparison to the brannerite phase. This supports the conclusion from XRD that brannerite becomes amorphous before zirconolite because of the occurrence of Pu-rich inclusions within the brannerite, which may possibly give brannerite a localized high-radiation field.

The dissolution rate for the Z1 material was found to be nearly independent of pH. We determined a forward dissolution rate of $1.7(4) \times 10^{-3}$ g/(m^2 d) for the Z1-239 specimen. This rate appears to be independent of Pu content. In our previous study [1], we showed that the dissolution rate is also independent of radiation-induced damage. However, equally possible is a mechanism in which a very insoluble alteration product on the surface forms on contact with water and controls the dissolution rate through some as yet to be determined rate limiting solution species.

Both ZB1 and ZIB1 ceramics were composed of the phases zirconolite, pyrochlore, and brannerite; ZB1-238 also contained excess PuO_2 that resulted from a make-up error, Hf-rutile, and Hf-srilankite. There was a rapid decrease in the 'true' density of the specimens with increasing dose at all storage temperatures. The 'true' density data indicate that the 'true' density decreases by 6.3% for the ZB1-238 specimens with no observed temperature dependence and 9.9%, 9.0%, and 8.6% for the ZIB1-238 specimens stored at 20 °C, 125 °C, and 250 °C, respectively. The radiation-induced swelling of the ZB1-238 specimens was 1.7% or a calculated bulk density decrease of 4.9%. Dimensional swelling in the ZIB1-238 specimens was 2.5% for a calculated decrease in the bulk density of 7.1%. The difference between the changes in the 'true' densities and the bulk swelling result from the conversion of open and accessible porosity to closed porosity with increasing radiation-induced swelling. There is a progressive loss of intensity in the XRD patterns and a general broadening of the diffraction peaks. In the ^{238}Pu-bearing specimens, brannerite appears to have become amorphous before the first XRD patterns were obtained. In both materials, zirconolite is the last phase to become amorphous, but it is unknown if this is because the zirconolite is more resilient to radiation-induced damage as indicated in the literature or if this particular phase has less of the total Pu than do the other phases. Brannerite would be expected to have the least Pu based on the thermodynamic instability of $PuTi_2O_6$ [43]. However, there must be sufficient Pu contained in this phase for it to become amorphous rapidly, or the phase is so sensitive to radiation-induced damage that the radiation from the surrounding α-bearing material causes the brannerite to become amorphous. As with the XRD patterns from the Z1 specimens, there is no evidence for a progression from zirconolite to pyrochlore to fluorite before the material becomes amorphous. These ceramics become amorphous before 930 days

(approximately 700 years when the dose comes from ^{239}Pu in the repository) or an average dose of 5×10^{18} α/g for the ZIB1-238 specimens. Although zirconolite and PuO_2 can be identified as crystalline phases in the ZB1-238 material, the material was largely amorphous at the end of the experiments (1246 days or an average of 4×10^{18} α/g; approximately 950 years from ^{239}Pu).

Quality SEM data on the ZB1-238 specimen was not possible; however, the phase distribution in the ^{239}Pu ceramic was very similar to the ^{238}Pu ceramic in this case. There were significantly more lamellae structures in these ceramics compared to the Z1-238 specimen. Based on SEM-EDS results, though not quantitative, it is likely that zirconolite becomes amorphous last because it has the least Pu of the phases capable of incorporating Pu.

Although these materials become amorphous at low doses, the specimens remained physically strong. To load the XRD specimen holder, the specimen had to be pushed against modeling clay to align it in the X-ray beam. Even after the radiation-induced swelling saturated, the specimens remained physically intact with no evidence for microcracking as was noted by Clinard and coworkers [8,48]. Based on our results from the other ceramics in this study [1] and the results presented here, the material remains physically and chemically viable for the disposition of surplus weapons-grade Pu.

References

[1] D.M. Strachan, R.D. Scheele, E.C. Buck, J.P. Icenhower, A.E. Kozelisky, R.L. Sell, R.J. Elovich, W.C. Buchmiller, J. Nucl. Mater. 345 (2005) 109.

[2] R.G. Dosch, A.W. Lynch, T.J. Headley, P.F. Hlava, Titanate waste forms for high level waste – an evaluation of materials and processes, in: J.G. Moore (Ed.), Scientific Basis for Nuclear Waste Management, Plenum, Boston, MA, 1981.

[3] P.E.D. Morgan, A.B. Harker, J.F. Flintoff, T.M. Shaw, D.R. Clarke, Developments in SRP 'composite' defense ceramic radwaste forms, in: P.E.D. Morgan, A.B. Harker, J.F. Flintoff, T.M. Shaw, D.R. Clarke (Eds.), Advances in Ceramics, American Ceramic Society, Westerville, OH, 1984, p. 234.

[4] A.E. Ringwood, S.E. Kesson, N.G. Ware, Immobilization of U.S. defense nuclear wastes using the Synroc process, in: C.J.M. NorthrupJr. (Ed.), Scientific Basis for Nuclear Waste Management, Plenum, Boston, MA, 1980, p. 265.

[5] G.R. Lumpkin, J. Nucl. Mater. 289 (2001) 136.

[6] G.R. Lumpkin, K.L. Smith, R. Giere, Micron 28 (1997) 57.

[7] A.E. Ringwood, V.M. Oversby, W. Sinclair, The effects of radation damage on Synroc, in: C.J.M. NorthrupJr. (Ed.), Scientific Basis for Nuclear Waste Management, Plenum, Boston, MA, 1980, p. 273.

[8] F.W. Clinard, C.C. Land, D.E. Peterson, D.L. Rohr, R.B. Roof, Mater. Res. Soc. Symp. Proc. 6 (1982) 405.

[9] F.W. Clinard, L.W. Hobbs, C.C. Land, D.E. Peterson, D.L. Rohr, R.B. Roof, J. Nucl. Mater. 105 (1982) 248.

[10] W.J. Weber, H. Matzke, Radiat. Eff. 98 (1986) 93.

[11] W.J. Weber, J.W. Wald, H. Matzke, J. Nucl. Mater. 138 (1986) 196.

[12] G.R. Lumpkin, K.L. Smith, M.G. Blackford, R. Giere, C.T. Williams, Mater. Res. Soc. Symp. Proc. 506 (1998) 215.

[13] F.W. Clinard, D.E. Peterson, D.L. Rohr, L.W. Hobbs, J. Nucl. Mater. 126 (1984) 245.

[14] S.X. Wang, L.M. Wang, R.C. Ewing, G.S. Was, G.R. Lumpkin, Nucl. Instrum. and Meth. B 148 (1999) 704.

[15] K.L. Smith, N.J. Zaluzec, G.R. Lumpkin, J. Nucl. Mater. 250 (1997) 36.

[16] K.L. Smith, M.G. Blackford, G.R. Lumpkin, N.J. Zaluzec, Mat. Res. Soc. Symp. Proc. 608 (2000) 487.

[17] US Department of Energy (DOE). Report to Congress: Disposition of Surplus Defense Plutonium at Savannah River Site, Department of Energy, Washington, DC, 2002.

[18] US Department of Energy (DOE). Amended Record of Decision for the Surplus Plutonium Disposition Program, Office of the Federal Register, Washington, DC, 2002.

[19] D.M. Strachan, W.C. Buchmiller, W.R. Park, J.T. Munley, Instrum. Sci. Technol. 32 (2004) 1.

[20] D.M. Strachan, H.T. Schaef, M.J. Schweiger, K.L. Simmons, L.J. Woodcock, M.K. Krouse, Powder Diffr. 18 (2003) 23.

[21] J.P. Icenhower, D.M. Strachan, B.P. McGrail, R.A. Scheele, E.A. Rodriguez, J.L. Steele, V.L. Legore, Am. Miner. 91 (2006) 39.

[22] B.P. McGrail, W.L. Ebert, A.J. Bakel, D.K. Peeler, J. Nucl. Mater. 249 (1997) 175.

[23] D.M. Strachan, R.D. Scheele, J.P. Icenhower, A.E. Kozelisky, R.L. Sell, V.L. Legore, H.T. Schaef, M.J. O'Hara, C.F. Brown, W.C. Buchmiller, The status of Radiation Damage Experiments, PNNL-13721, Pacific Northwest National Laboratory, Richland, WA, 2001.

[24] L. Minervini, R.W. Grimes, K.E. Sickafus, J. Am. Ceram. Soc. 83 (2000) 1873.

[25] B.D. Begg, N.J. Hess, D.E. McCready, S. Thevuthasan, W.J. Weber, J. Nucl. Mater. 289 (2001) 188.

[26] R. Gieré, C. Hatcher, E. Reusser, E.C. Buck, Mat. Res. Soc. Symp. Proc. 713 (2002) 303.

[27] M.W.A. Stewart, E.R. Vance, A. Jostsons, K. Finnie, R.A. Day, B.B. Ebbinghaus, Mater. Res. Soc. Symp. Proc. 713 (2002) 381.

[28] S.D. Conradson, Appl. Spectrosc. 52 (1998) 252a.

[29] J.A. Fortner, A.J. Kropf, R.J. Finch, A.J. Bakel, M.C. Hash, D.B. Chamberlain, J. Nucl. Mater. 304 (2002) 56.

[30] J.A. Fortner, A.J. Kropf, A.J. Bakel, M.C. Hash, S.B. Aase, E.C. Buck, D.B. Chamberlain, Sci. Basis Nucl. Waste Manag. XXIII 608 (2000).

[31] M. Colella, G.R. Lumpkin, Z. Zhang, E.C. Buck, K.L. Smith, Phys. Chem. Miner. 32 (2005) 52.

[32] E.R. Vance, G.R. Lumpkin, M.L. Carter, D.J. Cassidy, C.J. Ball, R.A. Day, B.D. Begg, J. Am. Ceram. Soc. 85 (2002) 1853.

[33] E.C. Buck, B. Ebbinghaus, A.J. Bakel, J.K. Bates, Mater. Res. Soc. Proc. 465 (1997) 1259.

[34] B.D. Begg, E.R. Vance, R.A. Day, M. Hambley, S.D. Conradson, Mater. Res. Soc. Symp. Proc. 465 (1997) 325.

[35] H.F. Shaw, Determination of the Open and Closed Porosity in an Immobilized Pu Ceramic Wasteform, UCRL-ID-132605, Lawrence Livermore National Laboratory, Livermore, CA, 1998.

[36] L. Nasdala, J.M. Hanchar, A. Kronz, M.J. Whitehouse, Chem. Geol. 220 (2005) 83.

[37] L.B. Kong, J. Ma, W. Zhu, O.K. Tan, J. Alloys Comp. 335 (2002) 290.

[38] C.J. Howard, T.M. Sabine, J. Phys C: Solid State Phys. 7 (1974) 3453.

[39] B.T.M. Willis, The study of extended defects by X-ray and neutron diffraction, in: L. Eyring, M. O'Keeffe (Eds.), The Chemistry of Extended Defects in Non-Metallic Solids, North-Holland Publishing Company, Scottsdale, Arizona, 1969, p. 272.

[40] J.W. Wald, P. Offerman, Mater. Res. Soc. Symp. Proc. 11 (1982) 369.

[41] D.M. Strachan, R.D. Scheele, A.E. Kozelisky, R.L. Sell, H.T. Schaef, M.J. O'Hara, C.F. Brown, W.C. Buchmiller, Sci. Basis Nucl. Waste Manage. XXV 713 (2002) 461.

[42] F.W. Clinard, Am. Ceram. Soc. Bull. 65 (1986) 1181.

[43] K.B. Helean, A. Navrotsky, G.R. Lumpkin, M. Colella, J. Lian, R.C. Ewing, B. Ebbinghaus, J.G. Catalano, J. Nucl. Mater. 320 (2003) 231.

[44] P.K. Saripalli, B.P. McGrail, D.C. Girvin, Appl. Geochem. 17 (2002) 649.

[45] D.M. Strachan, R.D. Scheele, J.P. Icenhower, E.C. Buck, A.E. Kozelisky, R.L. Sell, R.J. Elovich, W.C. Buchmiller, Radiation Damage Effects in Candidate Ceramics for Plutonium Immobiliza-

tion: Final Report, PNNL-14588, Pacific Northwest National Laboratory, Richland, WA, 2004.
[46] G.R. Lumpkin, K.L. Smith, M.G. Blackford, J. Nucl. Mater. 289 (2001) 177.
[47] R.C. Ewing, T.J. Headley, J. Nucl. Mater. 119 (1983) 102.
[48] F.W. Clinard, D.L. Rohr, Spontaneous fragmentation of an alpha-active ceramic – A mechanism for dispersion of solid waste?, in: J.G. Moore (Ed.), Sci. Basis Nucl. Waste Manage., Plenum, NY, Boston, MA, 1981, p. 405.